IEEE Access
Multidisciplinary | Rapid Review | Open Access Journal

Received February 14, 2019, accepted February 21, 2019, date of publication February 28, 2019, date of current version March 18, 2019.

Digital Object Identifier 10.1109/ACCESS.2019.2901632

Investigation of a Stator-Ironless Brushless DC Motor With Non-Ideal Back-EMF

LIU YANG[1], JING ZHAO[1], (Member, IEEE), LEI YANG[2], XIANGDONG LIU[1], (Member, IEEE), AND LEI ZHAO[2]

[1]School of Automation, Beijing Institute of Technology, Beijing 100081, China
[2]Electromechanical Products Research and Development Center, Beijing Institute of Control Engineering, Beijing 100190, China

Corresponding authors: Jing Zhao (zhaojing_bit@bit.edu.cn) and Lei Yang (39718342@qq.com)

This work was supported in part by the National Natural Science Foundation of China under Project 51677005, in part by the Major Project of Zhongshan City under Grant 2016A1027, and in part by the Intelligent Equipment and Technology of Automation Research and Development Platform under Grant 2016F2FC007.

ABSTRACT This paper deals with the effects of permanent magnets (PMs) shapes and segmentation types on the trapezoidal degrees of the back electromagnetic force (EMF) and torque characteristics and rotor losses. The back-EMF waveforms with different PMs shapes and segmentation types are calculated through transient finite element method (FEM). It is found that the effects of PMs inward eccentricity and curvature have no influence on the shape of the back-EMF waveforms. The PMs asymmetrical segmentation with the middle sub-PMs applied with low magnetic energy product sintered ferrite magnet can obtain better trapezoidal back-EMF waveforms. Then, the torque characteristics and rotor losses of PMs' symmetrical and asymmetrical segmentations are investigated and evaluated. The results show that the PMs segmentation and applying low magnet energy product PMs of the middle sub-PMs can further improve the torque characteristics. Moreover, the outer PMs eddy current loss and rotor iron loss exhibit a great extent of decrement. Finally, a stator-ironless PM BLDC motor without the outer rotor PMs segmentation is manufactured and tested. The experimental results show good agreement with the FEM ones.

INDEX TERMS Stator-ironless, brushless DC (BLDC) motor, non-ideal back-EMF, rotor eddy current loss, permanent magnets (PMs) shape.

I. INTRODUCTION

As an indispensable branch of permanent magnet (PM) brushless DC (BLDC) machines, the stator-ironless PM BLDC machines have attracted much attention from researchers for their higher efficiency, lower mass, higher torque density, longer lifespan and more environmentally friendly than traditional iron-stator PM BLDC machines. Thus, the stator-ironless PM BLDC machines have brought prospect in a diverse range of applications, such as, attitude control systems of microsatellite in the aerospace industry [1]–[4] and flywheel energy storage system [5]–[7], distributed generation, power system peak load regulation [8] and electrical vehicles [9].

More electrical aircraft drive systems impose strict limits on efficiency and reliability. PM BLDC motors designed using high-energy PMs and operated at high speed helps reducing the physical size of the motor and improving the efficiency and reliability. Owing to the space constraint, the operation flux density is high, and because of high-speed operation, the frequency of the magnet flux wave is relatively high. Both these factors lead to high energy loss in the motor [3], [10]. The losses of the outer-rotor stator-ironless PM BLDC motor include two parts: the copper loss and the rotor eddy current loss. In general, the rotor eddy current loss is relatively small compared with the stator copper loss, and they are usually considered to be negligible in low- or moderate- speed stator-ironless PM BLDC motors [7]. However, the eddy current loss problem may be critical in high-speed PM BLDC motors equipped with surface-mounted PMs, in terms of the resulting temperature rise owing to the relatively poor heat dissipation from the rotor. In turn, this will result in partial irreversible demagnetization, particularly of sintered Neodymium Iron Boron (NdFeB) PMs, which have relatively high temperature coefficients of remanence and coercivity and a moderately

The associate editor coordinating the review of this manuscript and approving it for publication was Zhen Li.

high electrical conductivity. Additionally, the high temperature will intenerate the nonmagnetic stator frame and introduce a significant threat to safe operation of the motor. Hence, it is particularly important to consider the rotor eddy current loss at the design stage of the high-speed stator-ironless PM BLDC motors, not only gives better efficiency evaluation, but also prevent its excessive temperature rise and reduce the risk of partial demagnetization of the PMs.

As for the stator-ironless PM BLDC motor investigated in this paper, due to the inside-out motor design, there are no conductive shield and retaining sleeve on the PMs. The eddy currents may be induced in the PMs, the rotor back-iron and armature windings, by time and space harmonics in the air-gap field [11]–[13]. More specifically, the eddy currents result from: (i) stator magnetic motive force (MMF) harmonics which do not rotate in synchronous with the rotor. (ii) nonsinusoidal phase current waveforms, which result from six-step commutation and pulse-width modulation (PWM). Some techniques have been proposed to reduce the rotor eddy current loss, by decreasing the time harmonics of armature current [11], increasing the air-gap length [14], segmenting the PMs [15], or using multiphase windings [16]. However, these techniques also bring some drawbacks, such as decreasing the electromagnetic force (EMF) coefficient, distorting the air-gap field, and complicating the manufacturing process. The eddy current loss of an outer-rotor Halbach ironless PM BLDC motor is analyzed in [17], however, the Halbach designed PMs will excessively increase the cost of the motor, and not realistic in many current industrial applications. Compared with numerical methods, analytical method is easier to obtain insight, and consumes less time. However, with the powerful computational capabilities nowadays, the computational efficient numerical methods such as finite element analysis (FEA) has taken the main position [18], [19].

Besides, for PM BLDC motors, the torque ripple which is decided by the back electromotive force (EMF) and current waveforms is aggressive [20]. If the back-EMF is constant in the conduction region of current, the torque ripple will depends on the current ripple. In the ideal PM BLDC motors, the back-EMF waveform will be trapezoidal and the input voltage will be constant. However, due to the effect of the winding inductance and resistance, the current characteristics of actual PM BLDC motor are much different with the ideal case. So, the more trapezoidal of the back-EMF waveform, the small current ripple and torque ripple will obtained. In [21], the torque ripple is reduced by varying the input voltage for reducing current ripple. In [22], the currents in both two-phase conduction mode and commutation mode are adjusted based on the back-EMF waveforms, and the torque ripple reduction of the BLDC drives is achieved by controlling the currents of noncommutated windings to trace the optimized reference current.

In this paper, the effect of the back-EMF trapezoidal degrees on the output torque characteristics and rotor eddy current loss of the stator-ironless PM BLDC motor

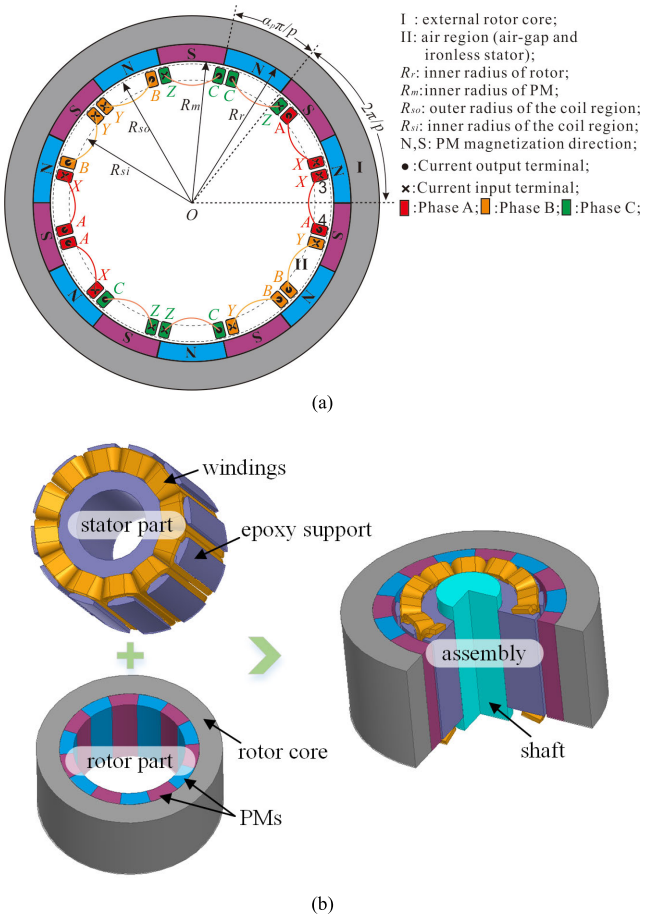

FIGURE 1. Analytical models of the presented stator-ironless PM BLDC motor. (a) 2-D model. (b) 3-D models.

is investigated. First, the specifications of the stator-ironless PM BLDC motor and analytical model is presented. Second, the back-EMF influence factors such as PM's shape and segmentation types are researched and discussed. Third, the torque and loss characteristics in terms of the current harmonics are calculated and evaluated through the finite element method (FEM). Finally, a stator-ironless PM BLDC motor prototype is manufactured and tested to validate the simulated results.

II. PROTOTYPE AND ANALYTICAL MODEL

A. PROTOTYPE OF THE STATOR-IRONLESS BLDC MOTOR

As for the high power density PM BLDC motor topologies, there are some other types, such as motors with inner back-iron of the rotor [7], motors with dual-rotor [1], [23] and motors with Halbach-array PMs [16]. Different motor types have been used on its corresponding situations to satisfy the specific requirements. The motor investigated in this paper is the structure simplest and the most widely used topology in many areas. Hence, the model as shown in Fig. 1 is chosen to investigate in this paper. The other stator-ironless PM BLDC motor topologies can be studied by the same way.

Fig. 1 (a) and (b) illustrate the 2-D and 3-D analytical models of the presented stator-ironless PM BLDC motor,

TABLE 1. Design parameters of the stator-ironless PM BLDC motor.

Symbol	Parameter	Value	Unit
p	Number of pole pairs	7	-
Q	Total number of slots	12	-
m	Number of phase	3	-
α_p	Magnet pole-arc to pole-pitch ratio	1	-
R_r	Inner radius of the rotor	28	mm
R_m	Inner radius of the PMs	25	mm
δ	The air gap length	0.5	mm
U_N	Rated voltage	14	VDC
P_N	Rated power	6	W
μ_r	Relative recoil permeability of the PMs	1.043	-
B_r	Remnant flux density of the PMs	1.28	T
I_{phase}	Rated phase current	1	A

respectively. Table 1 shows the detailed design parameters of the motor. It can be seen that the motor consists of an outer rotor part and an ironless stator part. The PMs are attached to the internal surface of the outer rotor core, with the magnet pole-arc to pole-pitch ratio equals to 1. Be limited by the space volume and the weight of the flywheel system, the PM BLDC driving motor is requested to be made as small and light as enough. As is well known, the stator winding configuration is determined by the slot-pole combination and the motor performance requirements. Concentrated windings are widely used to shorten the end windings and make the back-EMF more rectangular [24], [25]. As it can be seen from Fig. 1, the slot number per pole per phase and the pole pith of the motor investigated in this paper are 2/7 and 6/7, respectively. Hence, the coil pitch can just be 1 for this motor. The three phase concentrated windings can make the back-EMF more rectangular and axial end windings shorter than general permanent magnet synchronous motors.

B. THEORETICAL ANALYSIS

Three-phase PM BLDC motors are typically excited by 120° elec. deg. rectangular waveform currents under ideal conditions, as it shows in Fig. 2. And the phases of the back-EMF waveforms should be the same with the corresponding phase current and the 120° elec. deg. range should be flat too. However, the back-EMF waveforms are rather sinusoidal than square waves in fact. The torque of the BLDC motor with rectangular and sinusoidal back-EMF waveforms under the same drive mode are calculated and compared in ideal conditions.

For BLDC motors with rectangular back-EMF waveforms, the input current of each phase has the same phase with the back-EMF of the corresponding phase. And the back-EMF waveforms are with 120° elec. deg. flat tops in ideal conditions. So, the electromagnetic torque T_{rec} in one electric cycle can be expressed as (1).

$$T_{rec} = \frac{3\,(2 \times 120^{\circ})\,EI}{360^{\circ}} = 2\frac{EI}{\omega} \tag{1}$$

where, E and I are the amplitudes of the input phase currents and back-EMF, respectively. ω is the rotational speed.

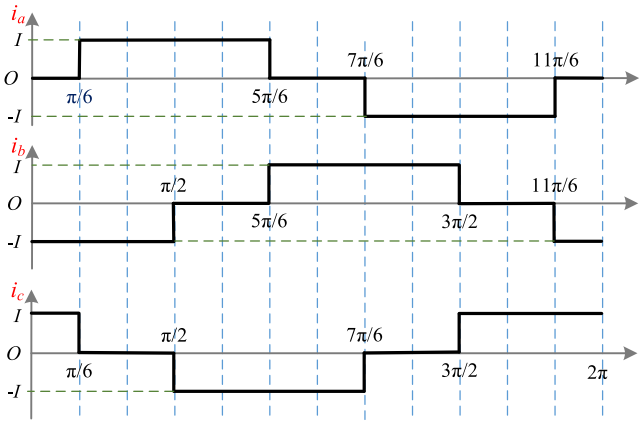

FIGURE 2. The three input phase currents for BLDC motors in ideal conditions.

For BLDC motors with sinusoidal back-EMF waveforms, the phase difference of the three phase currents (i_a, i_b, i_c) is 120 elec. deg. with each two adjacent phases (as illustrated in Fig. 2). The three phase back-EMFs (e_a, e_b, e_c) and current of phase A (i_a) can be expressed as (2) and (3), respectively.

$$\begin{cases} e_a = E\sin(\theta) \\ e_b = E\sin(\theta - 2\pi/3) \\ e_c = E\sin(\theta + 2\pi/3) \end{cases} \tag{2}$$

$$i_a = \begin{cases} 0 & [0, \pi/6) \\ I & [\pi/6, 5\pi/6] \\ 0 & (5\pi/6, 7\pi/6] \\ -I & (7\pi/6, 11\pi/6] \\ 0 & (11\pi/6, 2\pi] \end{cases} \tag{3}$$

where, E and I are the amplitudes of the phase back-EMF and input currents, respectively. θ is the rotation angle of the rotor.

Then, the electromagnetic power P_{sin} and torque T_{sin} of the BLAC motors can be expressed as (4).

$$\begin{aligned} T_{\sin} &= \frac{P_{\sin}}{\omega} = \frac{3}{6} \times \frac{e_a i_a}{\omega} \\ &= \frac{EI}{2\omega}\left[\int_{\frac{\pi}{6}}^{\frac{5\pi}{6}} \sin(\theta)\,d\theta - \int_{\frac{7\pi}{6}}^{\frac{11\pi}{6}} \sin(\theta)d\theta\right] \\ &= \sqrt{3}\frac{EI}{\omega} \end{aligned} \tag{4}$$

Comparing (1) and (4), it can be find that, under the same drive mode of rectangular waveform currents, the electromagnetic torque of BLDC motors with rectangular back-EMF waveforms T_{rec} is about 15.5% higher than that of the BLDC motors with sinusoidal back-EMF waveforms T_{sin}. Hence, in order to further improve the power density of the stator-ironless PM BDLC motor, the rectangular degree of the back-EMF should be greatly improved.

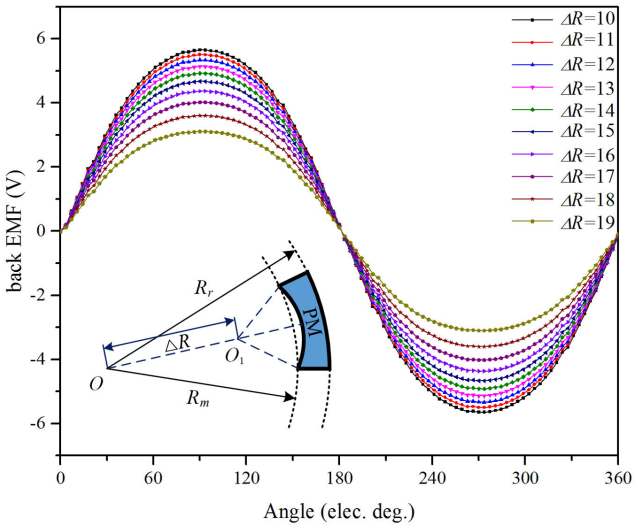

FIGURE 3. Back-EMF waveforms with different inward eccentricities of the PMs on the outer rotor.

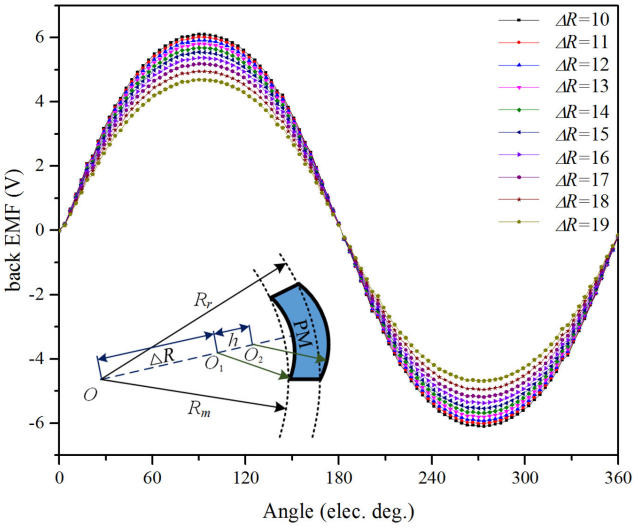

FIGURE 4. Back-EMF waveforms with different curvature of the PMs on the outer rotor.

III. FACTORS INFLUENCING TRAPEZOIDAL DEGREES OF BACK-EMF WAVEFORM

In order to improve the working efficiency and control accuracy, and reduce the power dissipation of the PM BLDC motor, one effective way is to improve the energy efficiency ratio. For this motor, it means adopting high performance magnetic materials, such as NdFeB or SmCo, to improve the power density. Beyond that, reducing the losses through structure optimization. From the derivation above, for BLDC motors, the more rectangular of the back-EMF 120° elec. deg. flat tops, the higher power density will obtained. The effect of the shapes and segmentation types of the outer rotor PMs are studied as follows.

A. OUTER ROTOR PMS SHAPE

1) PMS INWARD ECCENTRICITY

Fig. 3 shows the back-EMF with different PMs' inward eccentricities of the outer rotor. Compared to the inner rotor, the PMs' eccentricity for outer rotor is the inward type as shown in the left bottom of Fig. 3. $\triangle R$ is defined as the center distance of the circle O to O_1. The inner and outer diameters of the PM are kept consistent with the original design. Besides, the pole-arc to pole-pitch ratio α_p still remains to 1. As it can be seen that, the back-EMF waveforms are more sinusoidal than rectangular. The usage of the PMs is decreasing with the increasing of $\triangle R$, which cause the amplitude of the back-EMFs reducing in the meantime.

2) CURVATURE OF THE PMS

The PM with different curvature is shown at the left bottom of Fig. 4. O_1 and O_2 represent the centers of the inner and outer circles of the PM, respectively. $\triangle R$ is still defined as the center distance of the circles O and O_1. h is the center distance of the circles O_1 and O_2, and it keeps consistent with the thickness of the PM. As it can be seen from Fig. 4, the back-EMF waveforms along with different $\triangle R$ are much more sinusoidal than rectangular. And for a certain $\triangle R$, the amplitude of the back-EMF is bigger than that of in Fig. 3, due to more usage of the PM in this situation.

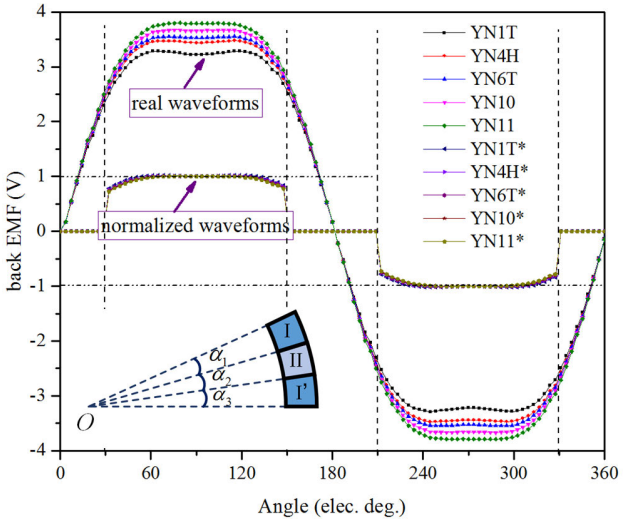

FIGURE 5. Back-EMF with all the PMs symmetrical segmented into three equal parts and the middle one with low magnetization intensity.

B. PMS SEGMENTATION TYPE

1) PMS SEGMENTED SYMMETRICALLY

In this part, the PMs are symmetrically segmented into three equal components. And the magnetization intensity of the three sub-PM blocks are not consistent with each other, the magnetic coercivity of the middle one is lower than the both sides of the adjacent two sub-PM blocks. As it shows in the left bottom of Fig. 5, the PM is separated into three parts, i.e., $\alpha_1 = \alpha_2 = \alpha_3 = 60/7$ mech. deg.. The sub-PM blocks I and I' are NdFeB, the middle ones are sintered ferrite magnets with relatively low magnetic energy. And the specifications of

TABLE 2. Specifications of the sintered ferrite magnets.

Grade	Remanence (mT)	Magnetic coercivity (kA/m)	Maximum magnetic energy product (kJ/m^3)	Conductivity (Siemens/m)
YN1T	63~68	50~70	0.8~1.2	
YN4H	135~155	85~105	3.2~4.5	
YN6T	180~220	120~140	5.0~7.0	-
YN10	220~240	145~165	9.2~10.6	
YN11	230~250	160~185	10.0~12.0	

the sintered ferrite magnets adopted in this paper, i.e. YN1T, YN4H, YN6T, YN10 and YN11, are listed in Table 2.

The real waveforms of the back-EMF with different sintered ferrite magnet of the middle sub-PM block is shown in Fig. 5. As it shows in Table 2, the magnetic coercivity of YN1T, YN4H, YN6T, YN10 and YN11 are 50∼70kA/m, 85∼105kA/m, 120∼140kA/m, 145∼165kA/m and 160∼185kA/m, respectively. However, the magnetic coercivity of sub-PM blocks I and I' is about 890kA/m, which is much higher than that of the sintered ferrite magnet II as it shows in the figure of the left bottom of Fig. 5. The real back-EMF waveforms are more trapezoidal than those of in Fig. 3 and Fig. 4. Which indicates that square-wave back-EMF can be obtained through the PM segmenting into three parts and the middle sub-PM block adopting lower magnet energy PM.

In order to better evaluate the rectangular degrees of the back-EMF waveform, the real waveforms of 30∼150 elec. deg. and 210∼330 elec. deg. are normalized. The values at 90° elec. deg. and 270° elec. deg. are chosen as the base values. The sintered ferrite magnet types with asterisk on the top right corner represent the normalized waveforms of the real back-EMF waveforms in Fig. 5. It can be observed that the normalized waveforms are almost the same with each other. Which indicates that the rectangular degrees of the back-EMF waveforms cannot be influenced by the magnetic coercivity of the middle sub-PM block.

2) PMS SEGMENTED ASYMMETRICALLY

The PMs are separated into three parts, as it shows in the left bottom of Fig. 6, the sub-PM blocks are labeled as ①, ②, ③, respectively. The middle one is sintered ferrite magnet type of YN1T, the other two sub-PM blocks are NdFeB. θ_1, θ_2, θ_3 represent the center angle of the sub-PM blocks ①, ②, ③, respectively. And $\theta_1 = \theta_3$, $\theta_1 + \theta_2 + \theta_3$ remains constant and equals to $\alpha_p \cdot \pi$/p. Here, $\theta_1 + \theta_2 + \theta_3 = 180/7$ elec. deg., θ_2 equals to 60°/7 mech. deg., 90°/7 mech. deg. and 120°/7 mech. deg.. The back-EMF waveforms with three different θ_2 are illustrated in Fig. 6, and the corresponding normalized waveforms are shown in the figure with asterisk on the top right corner of θ_2. In order to better demonstrate the normalized waveforms, a partial enlarged view of the normalize waveforms has been given below the normalized waveforms. It can be clearly seen that, the rectangle degree gets better with the increasing of the circle angle θ_2. However,

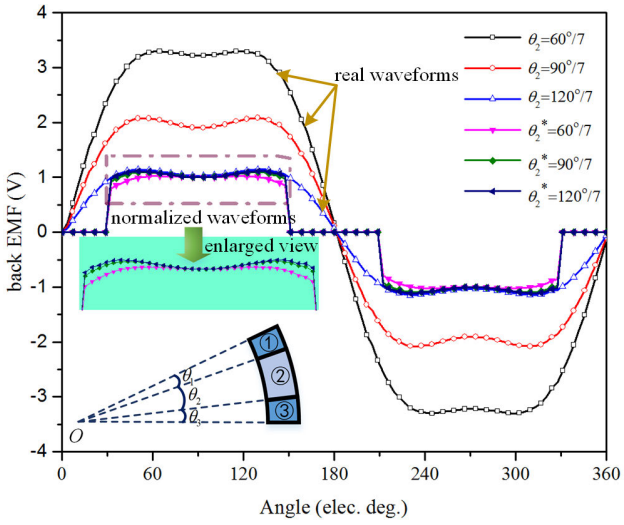

FIGURE 6. Back-EMF with all the PMs asymmetrical segmented into three parts and the middle one with low magnetization intensity.

TABLE 3. Variances of the back-EMF waveforms with three different angles of the middle PM.

	θ_2=60°/7	θ_2=90°/7	θ_2=120°/7
s^2	3.851‰	3.501‰	4.706‰

the normalized waveforms of $\theta_2^* = 90°/7$ and $\theta_2^* = 120°/7$ are very closed to each other, which indicates when the circle angle θ_2 reaches to a certain angle, the rectangular degree of the back-EMF will change little even though the circle angle θ_2 keep increasing continuously.

The back-EMF waveforms with other different angle of θ_2 can be obtained by the same way. The obtained waveforms as shown in Fig. 6 cannot include all the situations of different θ_2, it just give the variation tendency when the angle θ_2 increase from 60°/7mech. deg. to 120°/7mech. deg. with the step of 30°/7mech. deg.. In order to illustrate the rectangular degree of the back-EMF waveforms quantitatively. The variance of the three conditions is calculated and listed in Table 3. And the variance s^2 can be calculated as below.

$$s^2 = \frac{1}{n-1}\sum_{i=1}^{n}(1 - x_i)^2 \tag{5}$$

where, x_i is the value of ith quantity of the corresponding normalized back-EMF waveform.

As it can be seen, the variance of $\theta_2 = 90°/7$ mech. deg. is smaller than that of the other two types. However, the variance value of $\theta_2 = 60°/7$ mech. deg. is about 9% smaller than that of $\theta_2 = 90°/7$ mech. deg. And considering the manufacturing process and mechanical strength of the rotor PMs, the value of the angle θ_2 cannot too big. Or, the adjacent two sub-PMs (viz. PMs labeled ① and ③, as it shows in the left bottom of Fig. 6) cannot sustain high speed operations.

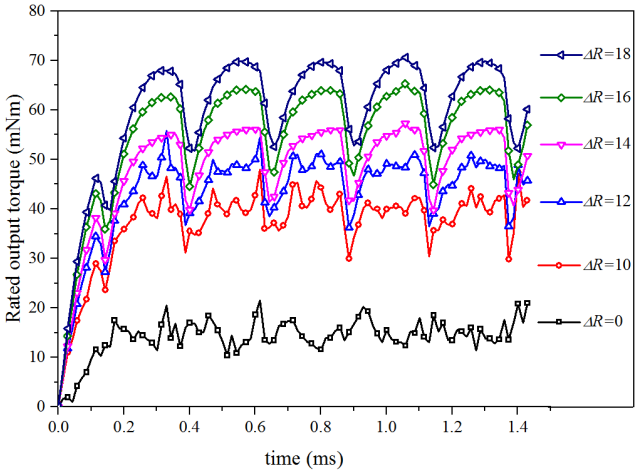

FIGURE 7. Rated output torque under full load conditions with different inward eccentricities of the outer PMs.

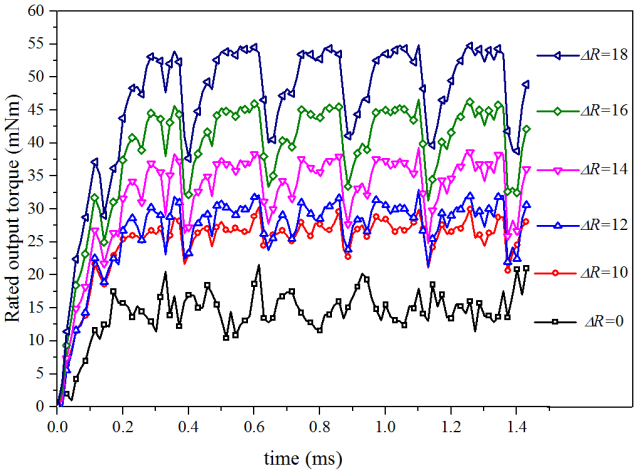

FIGURE 8. Rated output torque under full load conditions with different curvatures of the outer PMs.

TABLE 4. Rated output torque characteristics with different inward eccentricities of the outer PMs.

	ΔR=0	ΔR=10	ΔR=12	ΔR=14	ΔR=16	ΔR=18
average torque (mNm)	15.11	39.55	46.34	51.60	58.76	63.76
torque ripple (%)	36.76	23.05	21.11	16.97	17.63	14.80

TABLE 5. Rated output torque characteristics with different curvatures of the outer PMs.

	ΔR=0	ΔR=10	ΔR=12	ΔR=14	ΔR=16	ΔR=18
average torque (mNm)	15.11	26.47	28.53	34.43	41.54	49.58
torque ripple (%)	36.76	18.21	20.49	20.99	18.53	17.31

IV. TORQUE CHARACTERISTICS OF THE PM BLDC MOTOR

A. INFLUENCE OF OUTER ROTOR PMS SHAPE

Here, the emphasis is on the steady-state operation process, and the mechanical transient is ignored during the load output torque analysis. The transient simulation is performed at a rotational speed of 6000 r/min. Fig. 7 illustrates the rated output torque with different inward eccentricities of the outer PMs under full load conditions. And the corresponding specific torque characteristics, i.e. the average toque and torque ripple, are calculated and tabulated in Table 4. The torque ripple is calculated as below.

$$\zeta = \frac{T_{\max} - T_{\min}}{2 \cdot T_{avg}} \times 100\% \tag{6}$$

where, ζ is the torque ripple. $T_{\max}$ and $T_{\min}$ are the maximum and minimum torques in the steady state, respectively. T_{avg} is the average torque in the steady state.

It can be seen from Fig. 7 and Table 4 that, the average torque increases along with the increasing of $\triangle R$. The meaning of $\triangle R$ is described in detail in Section III-A. $\triangle R = 0$ means nothing was done with the outer PMs. In reverse, the torque ripple decreases with the increasing of $\triangle R$.

Similarly, the rated output torques under full load conditions with different curvatures of the outer PMs are calculated and illustrated in Fig. 8. And the corresponding rated output torque characteristics are calculated and tabulated in Table 5. The average torque and torque ripple are calculated in the steady state too. It can be found that, in this situation, the variation trend of the average torque and the torque ripple along with the increasing of $\triangle R$ is the same with the outer PMs of different inward eccentricities. That is, the average torque increases and the torque ripple decreases along with the increasing of $\triangle R$.

Comprehensive comparative analyze the effect of the inward eccentricities and curvatures of the outer PMs on the output torques, it can be found that, the average torques are increasing along with the increasing of $\triangle R$. It can be seen from Figs. 3∼4 that, the bigger of the $\triangle R$, the smaller of the back EMF will be obtained. And based on the ohm law, the armature current will be enlarged with the fixed bus voltage. Hence, though the flux density in the air region become smaller along with the increasing of $\triangle R$, the average torques still keep increasing.

B. INFLUENCE OF PMS SEGMENTATION TYPE

Fig. 9 shows the motor output torque with different rotational speed. It should be noted that, all the rotor PMs are symmetrically segmented into three components, as it shows in the left bottom of Fig. 5. In addition, the middle sub-PMs (viz. the sub-PM labeled "II" in Fig. 5) are sintered ferrite magnets of YN1T, which have relative low magnetic energy product than the other two adjacent sub-PMs (viz. the sub-PMs labeled "I" and "III" in the left bottom of Fig. 5). For the motor, the rated rotational speed is 6000 r/min, and the rated output torque is about 10mNm. As it can be seen form Fig. 9 that, when the output torque reaches to 10mNm, the rotational speed can even close to 9500 r/min, which is about 1.6 times

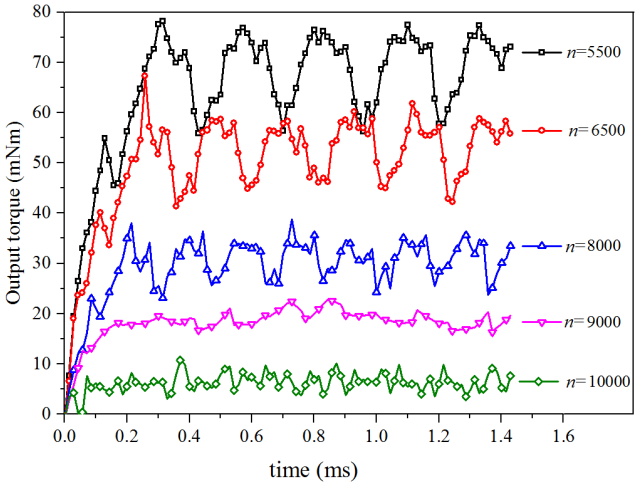

FIGURE 9. The output torque along with different rotational speed when the rotor PMs symmetrical segmented into three components and the middle one with low magnetization intensity.

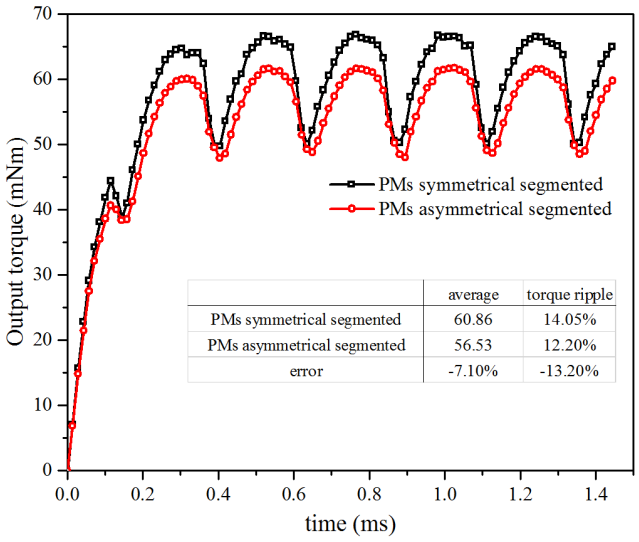

	average	torque ripple
PMs symmetrical segmented	60.86	14.05%
PMs asymmetrical segmented	56.53	12.20%
error	-7.10%	-13.20%

FIGURE 10. The output torque comparison with PMs symmetrical and asymmetrical segmented.

than that of the rated rotational speed. Similarly, when the rotational speed reaches to 6000 r/min, the output torque is about 60mNm, which is about 6 times than that of the rated output torque. This is mainly caused by the PM segmentation and the usage of the low magnetic energy product for the middle sub-PM, which result in low magnetic intensity of the direct-axis and helpful to flux-weakening capability.

Fig. 10 shows the output torque with PMs symmetrical and asymmetrical segmented types. And the corresponding values of the output torque graph is given in the table, which is located in the middle of Fig. 10. The physical dimension and the parameters of the two simulation models are identical with each other, except for the PMs segmentation type. For the PMs asymmetrical segmented (as it can be seen in Fig. 6), the central angle of the middle sub-PM θ_2 is 90°/7 mech. deg.. As it can be seen from Fig. 10 that, the average torque with the PMs symmetrical and asymmetrical segmented PM BLDC motors are 60.86mNm and 56.53mNm, respectively. This is mainly caused by the reduction of the magnetic flux density with the situation of PMs asymmetrical segmented.

Considering the steady operation state, the torque ripple with the PMs symmetrical and asymmetrical segmented PM BLDC motors are 14.05% and 12.2%, respectively. The back-EMF waveforms' variances of the PMs symmetrical and asymmetrical segmented types are 4.452‰ and 3.501‰, respectively. As it shows in Fig. 10, the error of the average output torque and the torque ripple are -7.1% and -13.2%, respectively. The negative sign represent the depressed value of the corresponding average torque and torque ripple from PMs symmetrical segmented to asymmetrical segmented. It indicates that, the torque ripple decreases with the reduction of the back-EMF waveform's variance. As the stator-ironless PM BLDC motor is used for the attitude control flywheel systems, the torque ripple is mainly considered. It can be seen that, the torque ripple decrease more than that of the average torque when the rotor PMs are asymmetrical segmented. Hence, the stator-ironless PM BLDC motor with rotor PMs asymmetrical segmented is more suitable for attitude control flywheel systems.

V. LOSSES OF THE PM BLDC MOTOR

According to the law of conservation of energy, the sum of the active power and the losses (which include the copper loss, iron loss, fraction loss and other stray loss) should keep consistent with the initial total energy. The active power and the losses are inversely proportional with each other, since the total energy is fixed. Thus, one effective way to increase the active power is to decrease the loss components of the motor. The fraction and stray losses are assumed to keep consistent under different operation conditions.

According to the ohms law, the copper loss P_{copper} of the phase windings can be calculated as below:

$$p_{copper} = \sum_{k=1}^{N} i_k^2 R_k \tag{7}$$

where, N is the number of winding phases (in this paper, $N = 3$). i_k is the current flowing in kth phase winding. R_k is the resistance of the corresponding kth phase winding.

The eddy current loss p_c in the outer rotor core or PMs can be calculated by [12]

$$p_c = \frac{1}{T}\int_0^T \int_V \frac{J_e^2}{\sigma} dvdt \tag{8}$$

where J_e is the current density And σ is the conductivity.

Because of the outer rotor core and the PMs are integrated as an integral whole and rotating synchronously, the alternating frequency f of the magnetic field excited by the PMs is zero. Hence, the losses in the outer rotor components caused by the magnetic field excited by the outer PMs can be neglected. However, the losses will be aggressive with the input rectangular phase currents, which consists of multi of harmonics.

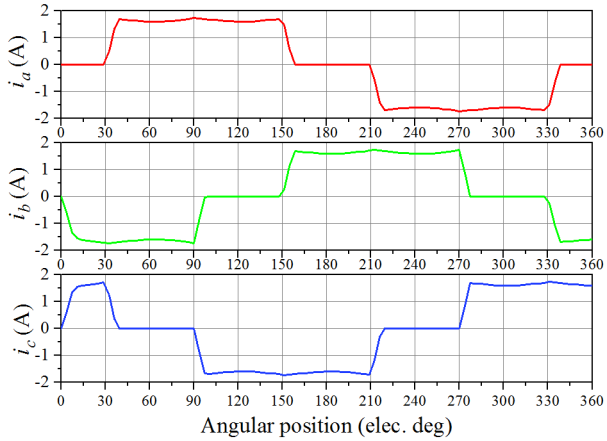

FIGURE 11. The simulated phase current waveforms of the stator-ironless PM BLDC motor at full load and rated rotational speed.

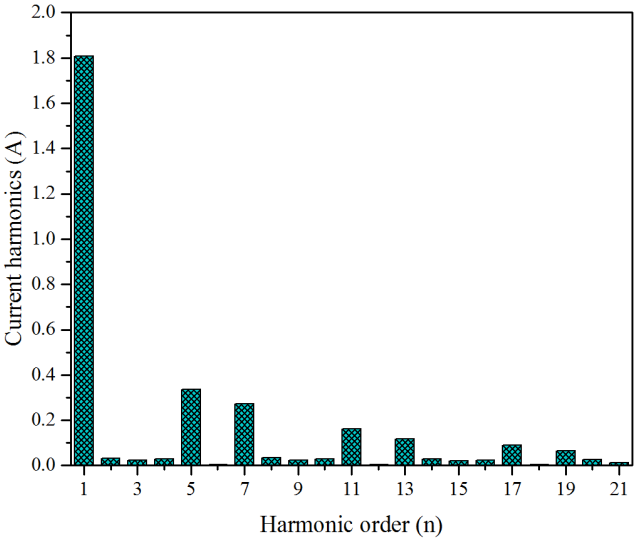

FIGURE 12. The rated phase current spectrum of phase A.

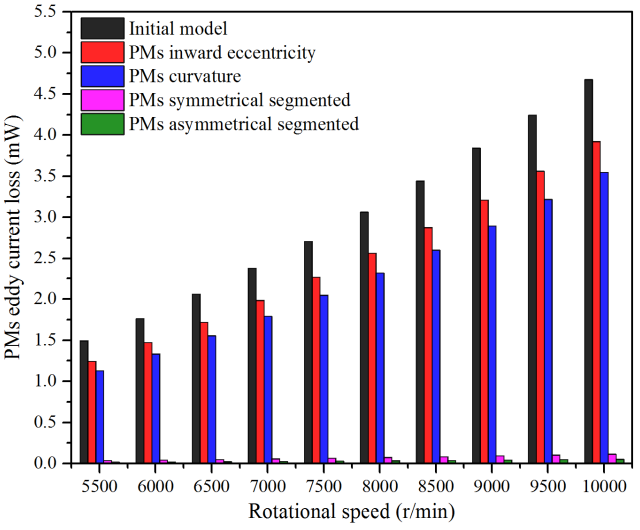

FIGURE 13. The PMs eddy current loss with different outer PMs shapes and segmentation types along with different rotational speed.

Generally, in high speed PM motors, winding losses and core loss will dramatically influence the motor's electromagnetic performance. The winding losses are caused by a combination of the following phenomena: skin effect, proximity effect, eddy current generated by rotation of rotor [26], and circulating current effect which is resulted from the inductance imbalance between the strands in a single branch, or caused by the imperfect manufacturing processing [27], [28].

From the analysis in the preceding sections, it is seen that the rotor eddy current loss is relatively low if compared with the motor power. However, the rotor eddy current loss may cause temperature rise in the rotor, such that the magnets may be demagnetized. Therefore, it is crucial to reduce the rotor loss. For this stator-ironless PM BLDC motor, the time harmonics of the armature current play a vital role in generating the rotor eddy current loss [29]. The rated three phase currents of the investigated stator-ironless PM BLDC motor are shown in Fig. 11. And the rated phase current spectrum of phase A, which is calculated by Fast Fourier Transform Algorithm, is shown in Fig. 12. As it can be seen, the major time harmonics are 5^{th}, 7^{th}, 11^{th}, 13^{th}, 17^{th}, 19^{th} orders.

A. PMS EDDY CURRENT LOSSES

The PMs eddy current loss with different outer PMs shapes and segmentation types along with different rotational speed, is analyzed with time-stepping transient FEM, as shown in Fig. 13. The conductivity of the rotor iron is set to zero during the calculation of the PMs induced eddy current loss. Some assumptions have to be made as below.

1) the inductances and resistances of the three phase windings are symmetrically distributed.
2) the windage loss and skin effect of winding conductors can be neglected.
3) the copper loss distributed evenly.
4) there is no imperfect manufacturing process and assembly error of the motors.

In order to compare the effects of four different PM variation cases on the PMs eddy current losses and the rotor iron loss, the cases of PMs inward eccentricity and PMs curvature are chosen of $\triangle R = 15$. As for the PMs with symmetrical and asymmetrical segmentations, the PMs are segmented into three components as it shows in the left bottom of Fig. 5∼6, respectively. The middle PMs labeled of II and ② are of sintered ferrite magnet YN1T. For the PMs asymmetrical segmented case (as it can be seen in Fig. 6), the central angle of the middle sub-PM θ_2 is selected to 90°/7 mech. deg. too. It can be seen from Fig. 13 that, the PMs eddy current loss with PMs without segmentation is much higher than that of PMs symmetrical and asymmetrical segmentations for each certain rotational speed. The PMs eddy current loss with each case of PMs without segmentation is nearly linear increasing

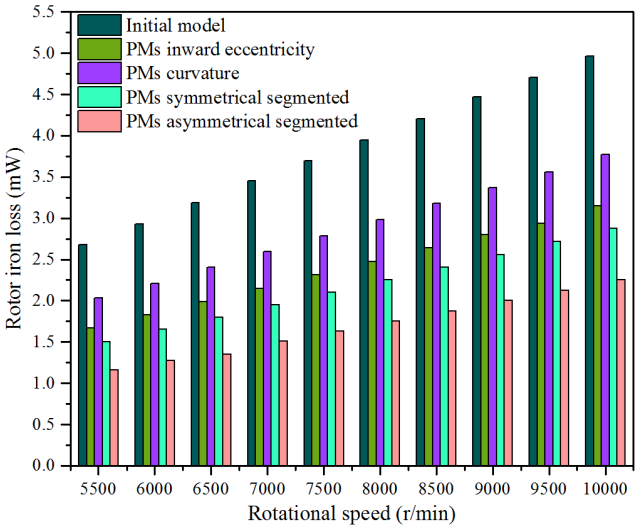

FIGURE 14. The rotor iron loss with different outer PMs shapes and segmentation types along with different rotational speed.

along with the rotational speed increasing. However, because of the effect of segmentation and the usage of non-conducting sintered ferrite magnet, the PMs eddy current losses with PMs symmetrical and asymmetrical segmented keep low and change little. It indicates that the PMs eddy current loss can be neglected if the PMs are segmented into three components and the middle one applied with low magnetic intensity.

B. ROTOR IRON LOSS

Similarly, the rotor iron loss with different outer PMs shapes and segmentation types along with different rotational speed is calculated and illustrated in Fig. 14. As it can be seen, the rotor iron loss is liner increasing along with the rotational speed of the five cases. And because of the field modulation of the PMs symmetrical and asymmetrical segmentation types, the increase amplitude with the condition of PMs of initial model is about 2.2 times higher than that of the PMs asymmetrical segmented. And on the whole, the rotor iron loss with segmented PMs is lower than that of the PMs without any segmentations. In addition, the rotor iron loss with PMs asymmetrical segmented is about 20% lower than that of the PMs symmetrical segmented. This is mainly caused by more sintered ferrite magnet adopted in the case of PMs asymmetrical segmented. Though the rotor iron loss is 2.2 times lower for each certain rotational speed when the PMs asymmetrical segmented, the rotor iron loss cannot be ignored during the motor design process.

VI. EXPERIMENTAL VERIFICATION

A prototype of the stator-ironless PM BLDC motor with parallel magnetized and no-segmented PMs is manufactured and tested. The stand platform with test and load stator-ironless PM BLDC motors is shown in Fig. 15. The experimental test system is shown in Fig. 16.

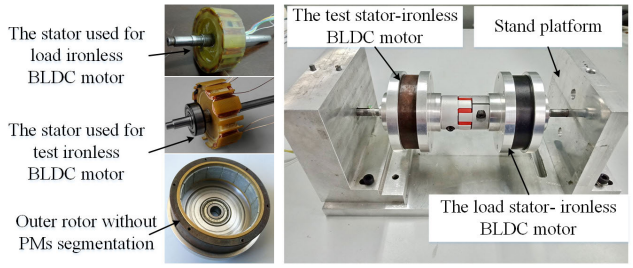

FIGURE 15. The stand platform with test and load stator-ironless PM BLDC motor without PMs segmentation.

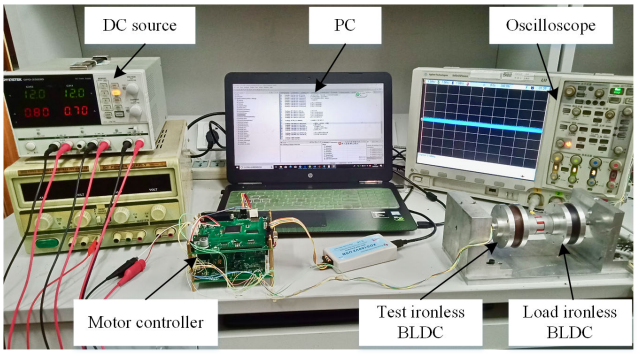

FIGURE 16. Experimental setup.

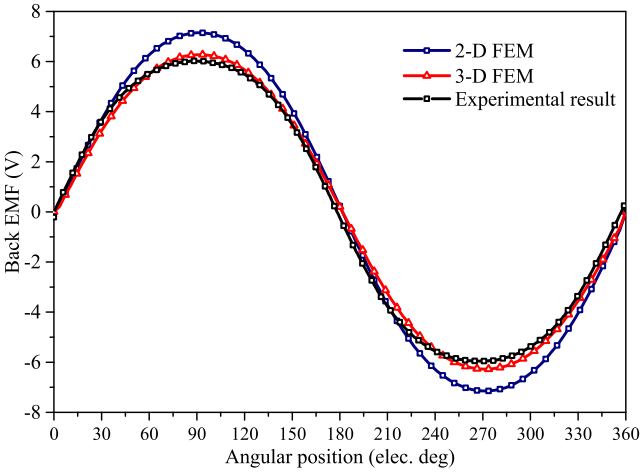

FIGURE 17. The simulated and experimental back EMFs of phase A.

The no-load back EMF waveform is obtained at the speed of 3800 r/min and compared with the FEM computation results, and are shown in Fig. 17. It can be seen that the result obtained from the 2-D FEM computation is about 15% higher than that of the experiment result. The 3-D FEM computational results which is account for the axial end effect and end windings have a good agreement with the experiment results. And the difference between the measured and calculated by 3-D FEM is about 4%. which thought to be caused by the PMs' magnetic field intensity in real motor topology and the position error of the coils.

VII. CONCLUSION

In this paper, the characteristics and effects of the outer rotor PMs inward eccentricity and curvature, PMs symmetrical and asymmetrical segmentations on the back-EMF waveforms trapezoidal degrees and torque characteristics and rotor losses were investigated. It was derived theoretically that the electromagnetic torque and power density of BLDC motors are higher than that of BLAC motors. Which indicates that the more trapezoidal of the back-EMF waveforms, the better performance the BLDC motors will exhibit.

The outer rotor PMs shapes and segmentation types on the back-EMF waveforms trapezoidal degrees were analyzed and discussed. It was found that the former has no impact on the back-EMF waveforms trapezoidal degrees improvement. The PMs asymmetrical segmentation could obtain better trapezoidal back-EMF waveforms, with the middle sub-PM applied relatively low magnet energy product magnets. Furthermore, the torque characteristics and rotor losses with rotor PMs segmentation and the middle sub-PMs applied with low sintered ferrite magnet were studied and discussed. The results showed that the PMs eddy current loss can be ignored during the motor design process. And the rotor iron loss cannot be ignored even though it could decrease 2.2 times lower than that of the PMs without segmentation. Finally, a prototype of the outer PMs without segmentation was manufactured and tested. The experimental results and the FEM results were compared and showed good agreement.

REFERENCES

[1] R. P. Praveen, M. H. Ravichandran, V. T. S. Achari, V. P. J. Raj, G. Madhu, and G. R. Bindu, "A novel slotless Halbach-array permanent-magnet brushless dc motor for spacecraft applications," *IEEE Trans. Ind. Electron.*, vol. 59, no. 9, pp. 3553–3560, Sep. 2012.

[2] X. Zhou and J. Fang, "Precise braking torque control for attitude control flywheel with small inductance brushless DC motor," *IEEE Trans. Power Electron.*, vol. 28, no. 11, pp. 5380–5390, Nov. 2013.

[3] S. De, M. Rajne, S. Poosapati, C. Patel, and K. Gopakumar, "Low-inductance axial flux BLDC motor drive for more electric aircraft," *IET Power Electron.*, vol. 5, no. 1, pp. 124–133, 2012.

[4] X. Zhou, X. Chen, F. Zeng, and J. Tang, "Fast commutation instant shift correction method for sensorless coreless BLDC motor based on terminal voltage information," *IEEE Trans. Power Electron.*, vol. 32, no. 12, pp. 9460–9472, Dec. 2017.

[5] J. Abrahamsson, J. Ögren, and M. Hedlund, "A fully levitated cone-shaped Lorentz-type self-bearing machine with skewed windings," *IEEE Trans. Magn.*, vol. 50, no. 9, pp. 1–9, Sep. 2014.

[6] W. Geng and Z. Zhang, "Investigation of a new ironless-stator self-bearing axial flux permanent magnet motor," *IEEE Trans. Magn.*, vol. 52, no. 7, Apr. 2016, Art. no. 8105104.

[7] K. Liu, X. Fu, M. Lin, and L. Tai, "AC copper losses analysis of the ironless brushless DC motor used in a flywheel energy storage system," *IEEE Trans. Appl. Supercond.*, vol. 26, no. 7, pp. 1–5, Oct. 2016.

[8] S. Li *et al.*, "Event-trigger heterogeneous nonlinear filter for wide-area measurement systems in power grid," *IEEE Trans. Smart Grid*, to be published. doi: 10.1109/TSG.2018.2810224.

[9] M. Z. Youssef, "Design and performance of a cost-effective BLDC drive for water pump application," *IEEE Trans. Ind. Electron.*, vol. 62, no. 5, pp. 3277–3284, May 2015.

[10] P. Ragot, M. Markovic, and Y. Perriard, "Optimization of electric motor for a solar airplane application," *IEEE Trans. Ind. Appl.*, vol. 42, no. 4, pp. 1053–1061, Jul./Aug. 2006.

[11] M. Zhang, W. Liu, and N. Zhao, "Estimation of eddy-current loss in surface mounted PM BLDC motor," in *Proc. ICEMS*, Aug. 2011, pp. 1–4.

[12] F. Zhou, J. Shen, W. Fei, and R. Lin, "Study of retaining sleeve and conductive shield and their influence on rotor loss in high-speed PM BLDC motors," *IEEE Trans. Magn.*, vol. 42, no. 10, pp. 3398–3400, Oct. 2006.

[13] N. Zhao, Z. Zhu, and W. Liu, "Rotor eddy current loss calculation and thermal analysis of permanent magnet motor and generator," *IEEE Trans. Magn.*, vol. 47, no. 10, pp. 4199–4202, Oct. 2011.

[14] I. Takahashi, T. Koganezawa, G. Su, and K. Ohyama, "A super high speed PM motor drive system by a quasi-current source inverter," *IEEE Trans. Ind. Appl.*, vol. 30, no. 3, pp. 683–690, May 1994.

[15] H. Toda, Z. Xia, J. Wang, K. Atallah, and D. Howe, "Rotor eddy-current loss in permanent magnet brushless machines," *IEEE Trans. Magn.*, vol. 40, no. 4, pp. 2104–2106, Jul. 2004.

[16] J. L. F. van der Veen, L. J. J. Offringa, and A. J. A. Vandenput, "Minimising rotor losses in high-speed high-power permanent magnet synchronous generators with rectifier load," *IEE Proc.-Electr. Power Appl.*, vol. 144, no. 5, pp. 331–337, Sep. 1997.

[17] K. Liu, M. Yin, W. Hua, Z. Ma, M. Lin, and Y. Kong, "Design and analysis of Halbach ironless flywheel BLDC motor/generators," *IEEE Trans. Magn.*, vol. 54, no. 11, Nov. 2018, Art. no. 8109305.

[18] K. Yoshida, Y. Hita, and K. Kesamaru, "Eddy-current loss analysis in PM of surface-mounted-PM SM for electric vehicles," *IEEE Trans. Magn.*, vol. 36, no. 4, pp. 1941–1944, Jul. 2000.

[19] S.-M. Jang, U.-H. Lee, D.-J. You, J.-P. Lee, and S.-H. Choi, "Operating torque estimation of high-speed slotless brushless DC machine considering power loss," *IEEE Trans. Magn.*, vol. 45, no. 10, pp. 4539–4542, Oct. 2009.

[20] G. Buja, M. Bertoluzzo, and R. K. Keshri, "Torque ripple-free operation of PM BLDC drives with petal-wave current supply," *IEEE Trans. Ind. Electron.*, vol. 62, no. 7, pp. 4034–4043, Jul. 2015.

[21] K.-Y. Nam, W.-T. Lee, C.-M. Lee, and J.-P. Hong, "Reducing torque ripple of brushless DC motor by varying input voltage," *IEEE Trans. Magn.*, vol. 42, no. 4, pp. 1307–1310, Apr. 2006.

[22] C. Xia, Y. Xiao, W. Chen, and T. Shi, "Torque ripple reduction in brushless DC drives based on reference current optimization using integral variable structure control," *IEEE Trans. Ind. Electron.*, vol. 61, no. 2, pp. 738–752, Feb. 2014.

[23] R. Qu and T. A. Lipo, "Dual-rotor, radial-flux, toroidally wound, permanent-magnet machines," *IEEE Trans. Ind. Appl.*, vol. 39, no. 6, pp. 1665–1673, Nov./Dec. 2003.

[24] X. Liu, H. Hu, J. Zhao, A. Belahcen, L. Tang, and L. Yang, "Analytical solution of the magnetic field and EMF calculation in ironless BLDC motor," *IEEE Trans. Magn.*, vol. 52, no. 2, Feb. 2016, Art. no. 8100510.

[25] X. Liu, H. Hu, J. Zhao, A. Belahcen, and L. Tang, "Armature reaction field and inductance calculation of ironless BLDC motor," *IEEE Trans. Magn.*, vol. 52, no. 2, Feb. 2016, Art. no. 8200214.

[26] D. A. Gonzalez and D. M. Saban, "Study of the copper losses in a high-speed permanent-magnet machine with form-wound windings," *IEEE Trans. Ind. Electron.*, vol. 61, no. 6, pp. 3038–3045, Jun. 2014.

[27] J. Fang, X. Liu, B. Han, and K. Wang, "Analysis of circulating current loss for high-speed permanent magnet motor," *IEEE Trans. Magn.*, vol. 51, no. 1, Jan. 2015, Art. no. 8200113.

[28] L. Yang, J. Zhao, X. D. Liu, A. Haddad, J. Liang, and H. Hu, "Effects of manufacturing imperfections on the circulating current in ironless brushless DC motors," *IEEE Trans. Ind. Electron.*, vol. 66, no. 1, pp. 338–348, Jan. 2019.

[29] Z. Q. Zhu, K. Ng, N. Schofield, and D. Howe, "Improved analytical modelling of rotor eddy current loss in brushless machines equipped with surface-mounted permanent magnets," *IEE Proc.-Electr. Power Appl.*, vol. 151, no. 6, pp. 641–650, Nov. 2004.

LIU YANG received the B.E. degree in machine design manufacture and automation from the Inner Mongolia University of Technology, Hohhot, China, in 2012, and the M.Sc. degree in mechanical electronic engineering from Harbin Engineering University, Harbin, China, in 2015. He is currently pursuing the Ph.D. degree with the School of Automation, Beijing Institute of Technology, Beijing, China.

His research interests include modeling and design of PM machines, and high-precision servo control for positioning systems.

JING ZHAO (M'13) received the B.Sc. degree from the Hebei University of Technology, Tianjin, China, in 2005, and the M.Sc. and Ph.D. degrees from the Harbin Institute of Technology, Harbin, China, in 2007 and 2011, respectively, all in electrical engineering.

She is currently an Associate Professor Lecturer with the School of Automation, Beijing Institute of Technology, Beijing, China. Her research interests include electric machines and drive systems used for renewable energy and special servo machines systems.

LEI YANG received the B.Sc. degree in electrical engineering from Zhengzhou University, Zhengzhou, China, in 2005, and the M.Sc. degree in precision instruments and machinery from Beihang University, Beijing, China, in 2008.

She is currently a Senior Engineer for electrical design with the Beijing Institute of Control Engineering, Beijing. Her research interests include electric machines and electromagnetism used for space attitude control mechanism.

XIANGDONG LIU (M'14) was born in Jingmen, China, in 1971. He received the M.S. degree in electrical engineering, and the Ph.D. degree in space engineering from the Harbin Institute of Technology, Harbin, China, in 1995 and 1998, respectively.

He is currently a Professor with the School of Automation, Beijing Institute of Technology, Beijing, China. His research interests include high-precision servo control, motor drive control, piezoceramics actuator drive and compensation control, sliding control, state estimation, and attitude control.

LEI ZHAO received the B.E. degree in electrical engineering and automation, and the M.Sc. degree in motor and electrical appliances from the Beijing Institute of Technology, Beijing, China, in 2008 and 2010, respectively, where he is currently pursuing the Ph.D. degree with the School of Automation.

He is also a Senior Engineer with the Beijing Institute of Control Engineering. His research interests include high-precision servo control, anti-disturbance control, and spacecraft attitude control actuator.